Reaction-diffusion system with Brusselator kinetics: Control of a quasiperiodic route to chaos

S. Chakravarti
Department of Chemical Engineering, University of Wisconsin at Madison, Madison, Wisconsin 53706

M. Marek
Department of Chemical Engineering, Prague Institute of Chemical Technology, Prague, Czech Republic

W. H. Ray
Department of Chemical Engineering, University of Wisconsin at Madison, Madison, Wisconsin 53706
(Received 12 December 1994; revised manuscript received 30 May 1995)

A methodology for controlling complex dynamics and chaos in distributed parameter systems is discussed. The reaction-diffusion system with Brusselator kinetics, where the torus-doubling route to chaos exists in a defined range of parameter values, is used as an example. Poincaré maps and singular value decomposition are used for characterization of quasiperiodic and chaotic attractors and for the identification of dominant modes. Tested modal feedback control schemes based on identified dominant spatial modes confirm the possibility of stabilization of simple quasiperiodic trajectories in the complex quasiperiodic or chaotic spatiotemporal patterns.

PACS number(s): 05.45.+b

I. INTRODUCTION

The discussion of problems connected with the development of a systematic framework for control of complex dynamics and chaos in distributed parameter systems is the subject of this work. The control of complex dynamics has significant practical implications [1]. Transition to chaos via the quasiperiodic route occurs in a number of hydrodynamic and other systems. Control of such transitions could be used to improve characteristics of process systems. The issue of chaos control in distributed parameter systems (DPS) has been discussed in several papers [2–5]. However, there do not appear to be studies that address the problem of controlling chaos when it occurs through the quasiperiodic route in a DPS. The focus of this effort is to explore the possibility of controlling the chaotic attractor in a distributed system to one of the quasiperiodic attractors, namely, tori from which it evolves based on an understanding of the underlying dynamics. Obviously this also encompasses the task of controlling the system to periodic or steady state solutions. The distributed parameter system considered is of the reaction-diffusion type with Brusselator kinetics. A quasiperiodic or torus-doubling route to chaos is known to exist in the selected region of parameter space [6]. In order to achieve the desired control objective, it was found useful to combine ideas from previous work in the area of control of chaos in lumped parameter systems (LPS) and low-dimensional maps, general methodology of identification and control of distributed parameter systems, and analysis of spatiotemporal patterns in distributed systems.

The organization of the paper is as follows. Section II is a brief literature survey of some of the relevant work in the aforementioned areas. Section III illustrates the characterization of nonlinear dynamics by means of Poincaré maps. The method of singular value decomposition (SVD) is employed to identify the dominant topos (spatial eigenfunctions), chronos (time-varying amplitudes), and the energy associated with each of the modes. The sensitivity to noise is also studied. Section IV gives examples of system responses to carefully chosen harmonic forcing functions. The theory and results of the feedback control strategy are presented in Sec. V. The overall conclusions are stated in Sec. VI.

II. LITERATURE REVIEW

Chen [7] provides a bibliography of the significant contributions in the area of control and synchronization of chaotic systems. A majority of the papers are devoted to lumped parameter systems. Ott, Grebogi, and Yorke (OGY) [8] developed an efficient method to control chaos. The key idea was to use feedback involving minute time-dependent perturbations of an available system parameter to stabilize one of the numerous unstable periodic orbits embedded within a strange attractor. This method can turn the presence of chaos into an advantage since by carefully choosing the small parametric perturbations a large variety of periodic motions can be generated. This strategy was successfully applied to experimental systems [9,10]. Subsequent works [11–17] utilized the extreme sensitivity of chaos to rapidly direct the system to a desired accessible state. The method of OGY [8] was also applied to the regulatory control problem arising in a chaotic nonisothermal continuous stirred tank reactor [18] and further generalized to generate aperiodic orbits [19]. Since the method uses the Poincaré map, parameter changes are discrete in time. To overcome some

of the limitations imposed by the discrete nature of the perturbations, Pyragas [20] developed a delayed feedback control scheme where the parameter changes were continuous. An experimental implementation of this technique has been achieved [21]. A number of papers have demonstrated the suppression of chaos by means of periodic perturbations [22–25] and noise [26].

Pecora and Carroll [27,28] studied the driving of stable nonlinear systems with chaotic signals. The key idea was to consider a compound dynamical system composed of two subsystems coupled in only one direction so that the behavior of the second was influenced by the first but not vice versa. The first subsystem was referred to as the *drive* while the second was referred to as the *response*. Conditions were derived under which it was possible to synchronize the chaotic behavior of the *response* subsystem with that of the *drive* subsystem. Pyragas [29] used a variation of this method for stabilizing aperiodic orbits in a strange attractor. The main difference was that the desired aperiodic behavior was recorded *a priori*. The behavior of the system was then synchronized with the prerecorded history. This technique of synchronization was successfully implemented on experimental systems (primarily electronic circuits with nonlinear oscillators) [27,30].

Relatively few papers [2–5] deal with the challenging problem of controlling chaos in a distributed parameter system. There have been instances of chaos control in complex distributed systems in nature [31]. For example, a dolphin swims much faster than allowed by turbulent water flow over its complex body shape for known values of its muscular propulsive force. The swimming speed was found to be consistent with laminar flow apparently induced by skin oscillations. Auerbach *et al.* [3] developed a feedback control scheme that required modeling the dynamics of only a few of the possibly infinite phase-space variables. It was implemented directly from time series data and was independent of the overall dimension of the phase space. Gang and Kaifen [4] studied a system characterized by the one-dimensional drift wave equation driven by a sinusoidal wave. Control of chaos was achieved by means of injecting negative feedback through a monochromatic wave or by pinning at a certain point in the spatial domain. Qin *et al.* [5] addressed the problem of controlling spatiotemporal patterns on a catalytic wafer. Information on the dominant spatial structures of the chaotic dynamics was obtained through the Karhunen-Loéve decomposition and used to develop a local modal feedback control.

In the more general area of identification and control of DPS, we mention contributions by Gay and Ray [32,33] and Chen and Chang [34]. Gay and Ray [32,33] had chosen an integral equation representation for the DPS rather than the conventional partial differential equation form and then applied the theory and properties of the singular value decomposition. One of the main uses of SVD was to identify the dominant modes in the infinite-dimensional DPS. This procedure worked successfully for linear adjoint and non-self-adjoint systems. By means of appropriate linearization strategies and model predictive control techniques such as dynamic matrix control (DMC), the SVD-based integral equation approach was shown also to work well for nonlinear DPS including chemical tubular reactors. Chen and Chang [34] presented an identification and control methodology for distributed systems with unknown nonlinear dynamics. The identification was performed via the Karhunen-Loéve decomposition. The control strategy used center manifold and normal form techniques from modern geometrical theories of dynamical systems to derive a nonlinear feedback that performed significantly better than linear feedback.

The understanding of the dynamics of spatiotemporal patterns is a key step in the development of a successful control strategy for the DPS. Turbulence viewed from the perspective of chaotic dynamics has been widely studied by researchers in fluid mechanics [35]. Sirovich employed the Karhunen-Loéve expansion technique to identify the dominant coherent structures that describe the dynamics of turbulent flow in systems with different geometries. He proposed the method of snapshots (originally introduced by Lorenz [36]) which enabled more efficient computation of spatial eigenfunctions, especially in the case of multidimensional systems. Broomhead and King [37] used singular value decomposition to successfully reconstruct the chaotic attractor using numerical data from the chaotic regime of the *Lorenz model*.

III. DYNAMICS

A. System description

The Brusselator reaction kinetic scheme is a standard model system used for the study of dissipative structures in nonlinear chemical systems [38] just as the Lorenz model serves as a basis for studies of chaotic behavior in simple models of turbulence. The reaction scheme involves the transformation of initial components A and B into products D and E through the reaction intermediates X and Y:

$$\begin{aligned} A &\xrightarrow{k_1} X, \\ B + X &\xrightarrow{k_2} Y + D, \\ 2X + Y &\xrightarrow{k_3} 3X, \\ X &\xrightarrow{k_4} E. \end{aligned}$$

The case of the Brusselator reaction occurring in a membrane reactor is studied in this work. It is assumed that the reactor remains isothermal. A possible reactor design is shown in Fig. 1. The reaction medium in the reactor is in a thin tube without radial variations in composition. The concentrations of A and B and of the products D and E in the reactor are controlled by a lateral semipermeable membrane between the reactor tube and the zoned chambers formed by the tube jacket. There are 19 such zoned chambers with concentrations being measured by sensors located at the midpoint of each zone. The only exceptions are the zones at either end which

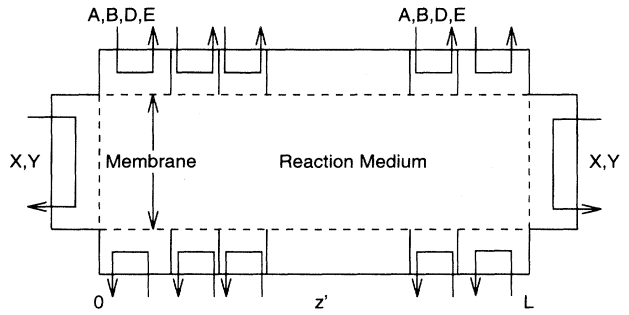

FIG. 1. Membrane reactor geometry.

are 1.5 times longer than the rest and have measurement sensors at the two-thirds point. Separate membranes at the end of the reactor control the concentration of intermediates X, Y at each end of the tube. There is no convective contribution so that the system could be alternately viewed as an infinite series of well mixed reaction cells coupled by diffusion. When the concentrations of A and B are considered constant and the concentrations of all components are made dimensionless so that they include the rate constants [38], the governing set of partial differential equations for the Brusselator kinetics in a reaction-diffusion system can be expressed as [6]

$$\frac{\partial X}{\partial t} = \frac{D_X}{L^2}\frac{\partial^2 X}{\partial z^2} + X^2Y - (B+1)X + A, \quad (1)$$

$$\frac{\partial Y}{\partial t} = \frac{D_Y}{L^2}\frac{\partial^2 Y}{\partial z^2} - X^2Y + BX. \quad (2)$$

The length of the reactor L is chosen as the bifurcation parameter. The diffusion coefficients D_X, D_Y of X and Y are chosen as 0.008 and 0.004, respectively. The dimensionless distance coordinate z ranges from 0 to 1. Also, A and B are 2.0 and 5.45, respectively. The boundary conditions are of the Dirichlet type:

$$X(t,0) = X(t,1) = \bar{X}, \quad (3)$$

$$Y(t,0) = Y(t,1) = \bar{Y}, \quad (4)$$

where $\bar{X}$ and $\bar{Y}$ are the steady state concentrations in the homogeneous system. A simple steady state calculation yields

$$\bar{X} = A = 2, \quad (5)$$

$$\bar{Y} = \frac{B}{A} = 2.725. \quad (6)$$

The infinite-dimensional distributed system needs to be projected onto a finite-dimensional system for purposes of computation of spatiotemporal data for dynamic analysis. This is achieved through a finite difference approximation where the spatial domain is discretized into P intervals of equal length so that the system of partial differential equations (PDEs) represented by Eqs. (1) and (2) reduces to a set of $2(P-1)$ ordinary differential equations (ODEs) in time represented by

$$\frac{dX_i}{dt} = \frac{D_X}{L^2h^2}(X_{i-1} - 2X_i + X_{i+1}) + X_i^2Y_i - (B+1)X_i + A, \quad (7)$$

$$\frac{dY_i}{dt} = \frac{D_Y}{L^2h^2}(Y_{i-1} - 2Y_i + Y_{i+1}) - X_i^2Y_i + BX_i, \quad (8)$$

where i varies from 1 to $(P-1)$. The boundary conditions (3) and (4) reduce to

$$X_0 = X_P = \bar{X}, \quad (9)$$

$$Y_0 = Y_P = \bar{Y}. \quad (10)$$

Integration of the set of ODEs then provides the solutions in the distributed (reaction-diffusion) system. Holodniok *et al.* [6] observed that the leading eigenvalues of the monodromy matrix, a measure of the stability of the periodic solution, were almost identical for $P = 20$ and $P = 40$. Also, we found the results of the simulations performed with $P = 40, 80, 160$ to be consistent with those for $P = 20$. Thus a discretization level of $P = 20$ suffices to capture the true behavior of the distributed system and hence is used throughout this work. However, the choice of time steps in the integration of Eqs. (7) and (8) proved to be a more subtle issue and is addressed later in this paper.

B. Poincaré maps

The nonlinear dynamics of interest can be studied by means of properly chosen Poincaré maps. Two approaches were employed for their construction. The first approach used the method described by Henon [39]. The key idea was to integrate the given set of ordinary differential equations until the trajectory crossed the Poincaré surface in a specific direction. Then, a single step in the reversed direction was taken with a slightly modified version of the differential equations to locate a point on the Poincaré surface. The procedure was implemented by means of a Runge-Kutta scheme (RKSUITE [40]). The second approach involved the use of DDASAC (double precision differential-algebraic sensitivity analysis code), developed by Caracotsios and Stewart [41], which has the capability to adaptively change the step size to locate the point exactly on the Poincaré surface. The underlying algorithm used in DDASAC is an extension of the DDASSL (double precision differential algebraic solver) predictor-corrector integrator [42]. Unless explicitly mentioned, it is to be assumed that the Poincaré maps presented in this work were constructed using DDASAC.

The Poincaré map for the present problem essentially represents the intersection of the trajectory of (7) and (8) and a $[2(P-1)-1]$-dimensional hypersurface suitably defined. For example, the surface could be defined by an equation of the form

$$X_{z=0.3}(t) = 2.0, \quad (11)$$

with $dX_{z=0.3}(t)/dt > 0$. The Poincaré map would then contain only those spatial profiles which satisfy the requirement of Eq. (11) as denoted by solid lines in Figs. 2(a) and 2(b). Because of the discrete approximation to the infinite-dimensional DPS, the profiles here are obtained by piecewise linear interpolation between 41 points. To represent the Poincaré map in two dimen-

sions it becomes necessary to project the map onto two chosen phase-space coordinates, i.e., concentrations of X and Y at chosen location in the reactor. The concentrations of X and Y at $z = 0.5$ when the concentration of X at $z = 0.3$ is 2.0 and increasing (see points Q and R in Fig. 2) were used here.

In such a two-dimensional (2D) map, a single point denotes periodic behavior. A closed orbit indicates quasiperiodic behavior (or torus) while a double closed orbit would suggest a torus doubling.

While constructing Poincaré maps for distributed systems, two issues arising from the high dimensionality need to be addressed.

(1) Choice of the Poincaré surface, i.e., if the Poincaré surface is defined as $X_{z=\zeta}(t) = a$ what does one choose for ζ and a?

(2) Choice of two phase-space coordinates onto which the Poincaré map can be projected for purposes of representation, i.e., if the concentration of X or Y satisfies the aforementioned requirement at $z = \zeta$, where does one measure the concentrations of X and Y?

The approach adopted was to generate Poincaré maps corresponding to different surfaces and take projections of each map at a number of locations. For all locations and surfaces studied the qualitative dynamics observed were consistent.

Subsequently, the philosophy was to choose a surface and a location so that one could best illustrate the dynamics of interest, which in this case was a cascade of torus doublings eventually leading to the evolution of a strange attractor [6]. Most 2D Poincaré maps presented in this work physically refer to the plot of concentrations of X and Y at the midpoint of the reactor when the concentration of X at $z = 0.3$ is 2.0 and increasing.

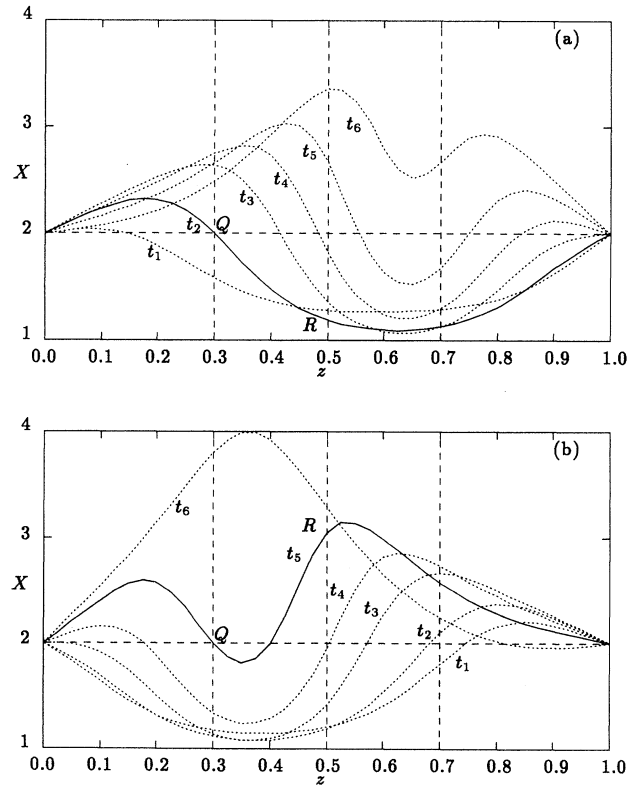

FIG. 2. Selecting spatial profiles for Poincaré maps of DPS. (a) and (b) correspond to initial conditions A and B (see text). $t_1 < t_2 < t_3 < t_4 < t_5 < t_6$. Equation (11) defines the Poincaré surface.

Equations (7) and (8) were integrated using two sets of initial conditions. The first set of initial conditions, denoted by A (or IC-A) throughout this paper, corresponds to:

$$X = 2.32,\ Y = 1.75 \text{ for } z < 0.5,$$

$$X = 3.32,\ Y = 2.75 \text{ for } z \geq 0.5.$$

The second set of initial conditions, referred to as B (or IC-B) is the mirror image of the initial condition A, i.e.,

$$X = 3.32,\ Y = 2.75 \text{ for } z < 0.5,$$

$$X = 2.32,\ Y = 1.75 \text{ for } z \geq 0.5.$$

The Poincaré maps that result as L is varied from 1.403 to 1.43 are presented in Fig. 3. The two-dimensional plots are essentially projections of the map at $z = 0.5$, corresponding to the Poincaré surface defined by Eq. (11) with the restriction that $dX_{z=0.3}(t)/dt > 0$. The attractors in the top left corner of each of the plots in Fig. 3 are obtained when initial condition A is used while the ones on the bottom right corner correspond to the initial condition B. The time steps in the vicinity of the Poincaré surface were of the order of 10^{-4} sec. A subroutine from RKSUITE [40] with automatic step size control (10^{-4} sec or less) yielded identical results (i.e., Fig. 3). Larger time steps yielded integration error and a set of Poincaré maps as shown in Fig. 4. One notes that the attractors corresponding to initial condition A are unaffected, but the attractors corresponding to initial condition B now seem to represent a sequence of highly wrinkled tori. Thus it is necessary to carefully choose the time step in order that the dynamics of the discretized system represent the actual behavior of the original system. This numerical artifact could have quite easily gone unnoticed had one not used both initial conditions.

The Poincaré maps in Figs. 3 and 4 reveal the existence of two coexisting and mutually mirror-symmetric spatially asymmetric attractors. The symmetry arises from the symmetry in the geometry of the problem and the solution reached depends on the initial conditions used. Also, the coexisting attractors show different sensitivities to different initial conditions as is reflected in the requirements on the control of the time steps. The attractors will henceforth be referred to as A or B as per the initial condition.

The significance of these attractors in the context of the spatial profiles can be better understood by turning to Fig. 2. If the simulations commence with the initial condition A, then the Poincaré map consists of spatial profiles of the type denoted by a solid line in Fig. 2(a)

where the concentration of X at the midpoint is less than 2.0. Such profiles then correspond to the attractors in sequence A. Similarly, the attractors in sequence B correspond to the spatial profiles of the form denoted by a solid line in Fig. 2(b) where the concentration of X at the midpoint is greater than 2.0.

Closer inspection of Fig. 2(a) would indicate that, if one were to consider a sequence of profiles, there always exists a time when the profile satisfies the condition $X_{z=0.7}(t) = 2.0$. The concentration of X at the midpoint being greater than 2.0 at that instant indicates that an attractor belonging to sequence B would be observed on this surface. The same reasoning applied to Fig. 2(b) would suggest that an attractor of type A would be observed if the surface were defined as $X_{z=0.7}(t) = 2.0$. This was confirmed by performing simulations for a particular set of initial conditions with both surfaces, i.e., $X_{z=0.7}(t) = 2.0$ and $X_{z=0.3}(t) = 2.0$. Thus instead of using symmetric sets of initial conditions to track the two coexisting and mutually mirror-symmetric attractors, one could simply use a fixed set of initial conditions but observe the map with respect to two surfaces so chosen that if the first one is $X_{(z=\zeta)}(t) = a$, the second is $X_{(z=1-\zeta)}(t) = a$. Also, if instead of the midpoint one chose to monitor the concentrations of X and Y elsewhere, for example at $z = \xi$, the relationship between the attractors with respect to different surfaces still holds with the added restriction that when switching the surface from $z = \zeta$ to $z = 1 - \zeta$, one also changes the location at which X and Y concentrations are monitored from $z = \xi$ to $z = 1 - \xi$. This aspect of the mirror symmetry implies that the different sensitivities of the attractors to different initial conditions could alternately be interpreted in terms of varying sensitivity with spatial location.

C. Singular value decomposition

The purpose of employing the singular value decomposition is twofold: (1) To analyze the dynamics of the spatiotemporal patterns and corroborate the finding of coexisting and mutually mirror-symmetric attractors, and (2) to provide information that could be the basis for a suitable control strategy.

Spatiotemporal patterns can be better understood if they are decomposed into time-independent spatial structures and their time-varying amplitudes. This orthogonal decomposition can be accomplished by means of the singular value decomposition. The reader is referred to the paper by Stewart [43] for detailed theory on the existence and properties of SVD. Implementation of SVD in this context (see Appendix) is in principle similar to the Karhunen-Loéve expansion [44,45], also referred to as proper orthogonal decomposition [35,46–48], biorthogonal decomposition [49], or method of empirical orthogonal functions [50]. The SVD analysis is applied to both reactants X and Y. Since the observed qualitative trends

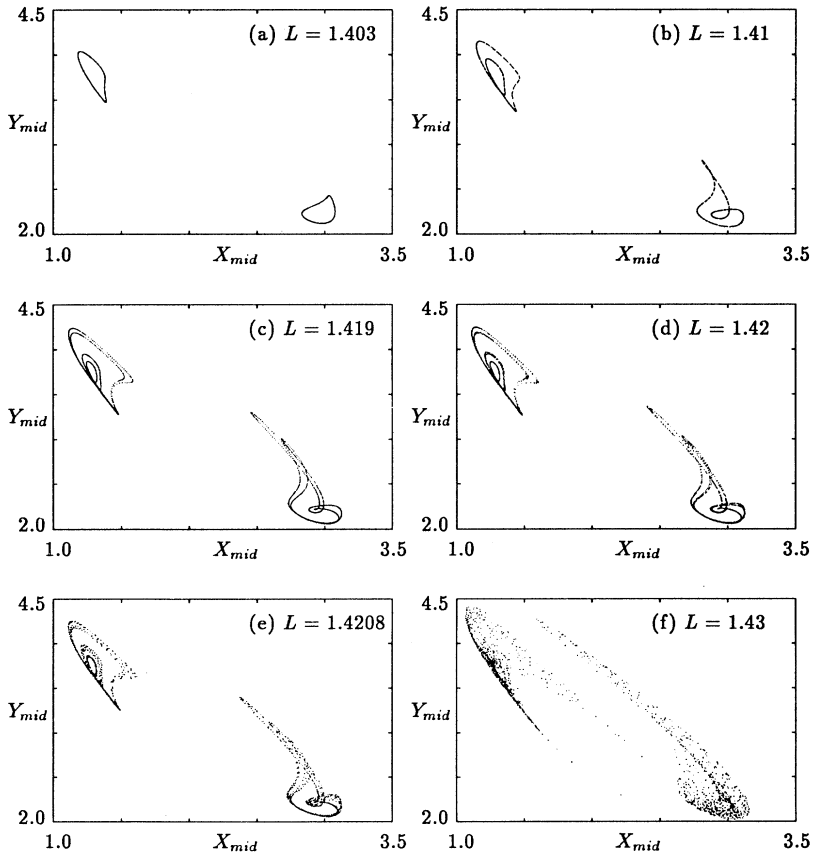

FIG. 3. Poincaré maps. The horizontal and vertical axes represent the concentration of X and Y at the midpoint, $z = 0.5$. The attractors in the top left corner are obtained using initial condition A while the ones in the bottom right correspond to initial condition B. Equation (11) defines the Poincaré surface.

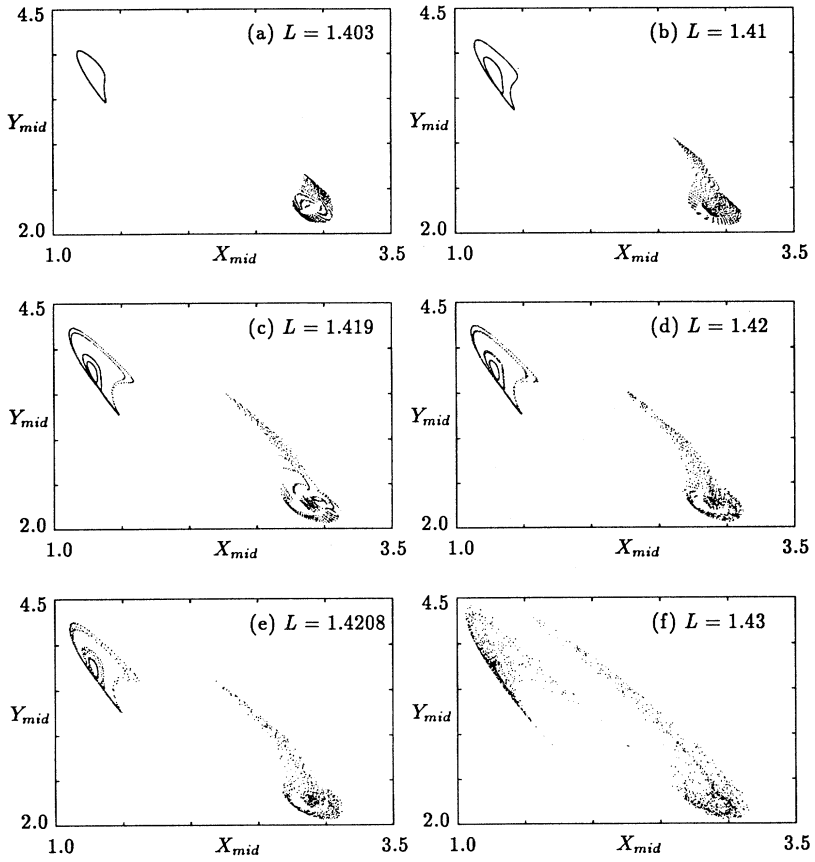

FIG. 4. Wrinkled Poincaré maps due to larger time steps. The horizontal and vertical axes represent the concentration of X and Y at the midpoint, $z = 0.5$. The attractors in the top left corner are obtained using initial condition A while the ones in the bottom right correspond to initial condition B. Equation (11) defines the Poincaré surface.

for X and Y were identical, the ensuing discussion is restricted to X. The implementation details are provided in the Appendix. It suffices to say here that the singular value decomposition of the spatiotemporal data, represented by a matrix, yields left and right (unitary) singular matrices and a diagonal singular value matrix. Following the terminology of Aubry *et al.* [49], the left and right singular vectors (i.e., the columns of the left and right singular matrices) will henceforth be referred to as topos and chronos (normalized, in this work), respectively.

Figure 5 illustrates the behavior of the topos, $\mathbf{w_i}(z)$, and $\mathbf{w_i^\star}(z)$, corresponding to initial conditions A and B, respectively, for the first four modes ($i = 1$ to 4). Note that the topos also retain the symmetry of the coexisting asymmetric attractors and are related by an expression of the form

$$\mathbf{w_i^\star}(z) = \mathbf{w_i}(1 - z). \tag{12}$$

The $(z, 1 - z)$ relation indicates that the symmetry is of the same mirror-image type seen in the Poincaré maps. The topos $\mathbf{w_i}(z)$ are inherent properties of the system and were found to fluctuate very little as L was varied. The consistency of the topos thus suggests their possible use in the development of a successful control strategy.

Field and Golubitsky [51] have demonstrated the existence of two symmetric period-doubling cascades for an odd logistic map of the form

$$g(x) = \lambda x(1 - x^2). \tag{13}$$

In the current context, their results are tantamount to asserting that the time-averaged spatial profiles for the two

TABLE I. Singular values — a measure of the energy content of the different modes.

	Singular values	
Mode	Torus ($L = 1.403$)	Chaos ($L = 1.43$)
1	48.20	48.34
2	18.25	18.24
3	7.19	8.72
4	3.36	5.64
5	2.91	3.45
6	1.49	2.17
7	0.97	1.24
8	0.67	0.81
9	0.37	0.45
10	0.24	0.33
11	0.14	0.19
12	0.10	0.13
13	0.06	0.08
14	0.04	0.05
15	0.03	0.04
16	0.012	0.024
17	0.011	0.013
18	0.003	0.008
19	0.001	0.002

mutually mirror-symmetric attractors at a given value of L are related as in Eq. (12). This was indeed the case as confirmed by further calculations. An example of the time-averaged profiles for the case $L = 1.403$ for initial conditions A and B is shown in Fig. 6. In principle, this was to be expected since the time-averaged spatial profile is essentially a linear combination of the topos.

From the square of the singular values, the relative energy of each mode can be assessed. The singular values are arranged in descending order, which implies that the first mode has maximum energy content, the second mode has the next highest energy content, and so on. Table I represents the singular values obtained for $L = 1.403$ and $L = 1.43$. About 85% of the energy is concentrated in the first mode itself and another 12% in the second mode. Also the distribution of the energy among the dominant modes remained similar throughout the regime of transition to chaos, i.e., $L = 1.403$ to 1.43. This observation coupled with the robustness of the topos lends support to the idea that, in a feedback control framework, desirable performance could be achieved by controlling the first mode alone.

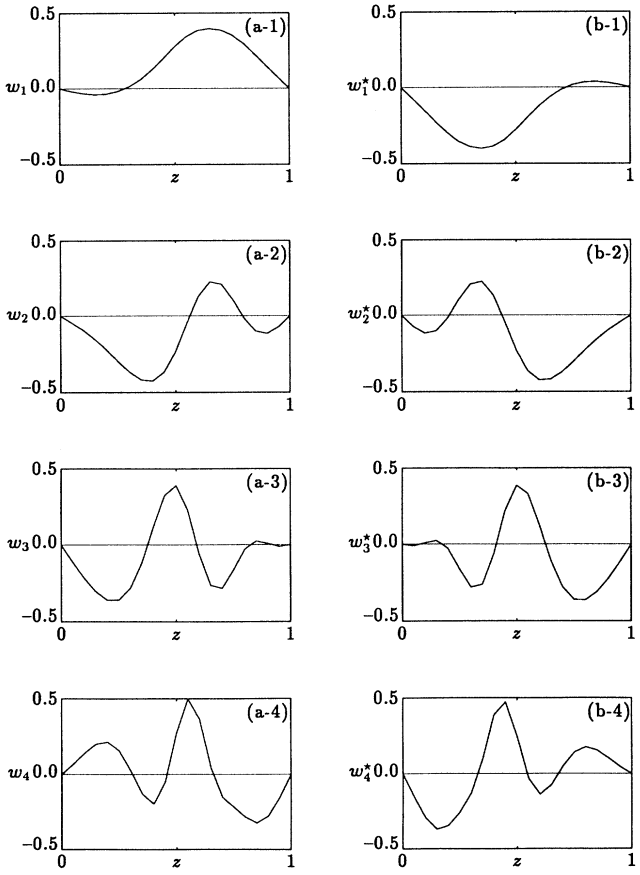

FIG. 5. Spatial eigenfunctions (topos) for modes 1–4 with $L = 1.403$. The letters "a" and "b" in parentheses at the top right corner of each plot indicate use of initial condition A and B, respectively, while the number denotes the corresponding mode. The horizontal axes denote the distance coordinate while the vertical axes represent the magnitude of the topos.

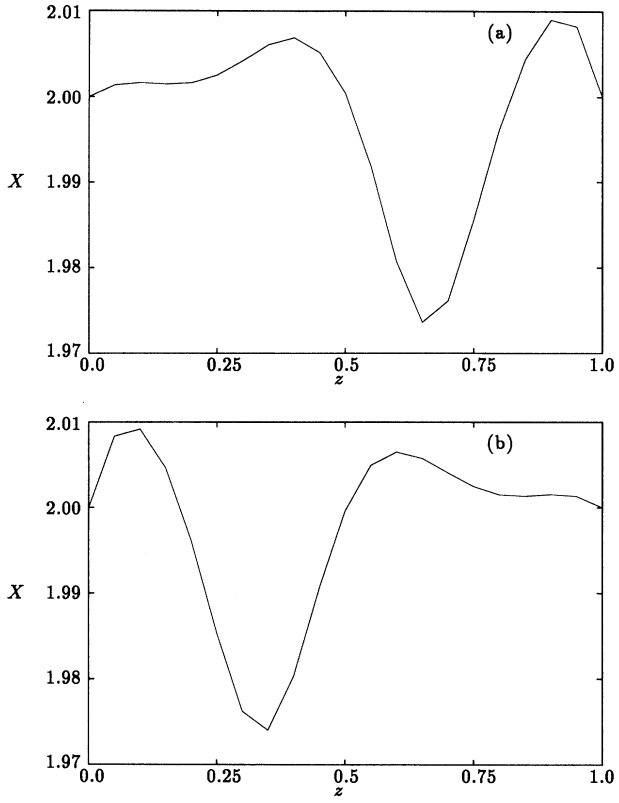

FIG. 6. Time-averaged spatial profiles corresponding to the 1-torus [Fig. 3(a)]. (a) and (b) correspond to initial conditions A and B, respectively. The horizontal axes represent the distance coordinate z while the vertical axes correspond to the concentration of X.

Since the topos remain virtually unchanged, it is to be expected that the transition to chaos would be manifested in the chronos. In order to obtain information more easily, the power spectrum of each chronos is presented rather than the corresponding time series. The results for the cases of 1-torus [$L = 1.403$, Fig. 3(a)] and chaotic attractor [$L = 1.43$, Fig. 3(f)] with initial condition A are shown in Fig. 7. The power spectrum of the first mode in both cases indicates that the most dominant frequency of the system is slightly less than 0.3 Hz while the second most dominant frequency is slightly greater than 0.4 Hz. This corresponds to two characteristic frequencies of the torus. For the second mode there exist in addition to peaks at the same two frequencies as the first mode a few other peaks, albeit much smaller in magnitude. The transition to chaos is best explained by the third and fourth modes. The torus displays a number of distinct peaks while for the chaotic case sections with much more closely located peaks are observed. Thus the power spectra indicate that the contribution to chaos comes from the relatively low energy modes.

The sensitivity of the SVD to noise was studied. White noise with zero mean and different variances was added to the spatiotemporal data prior to performing the SVD. As the variance increased, the topos and chronos got more

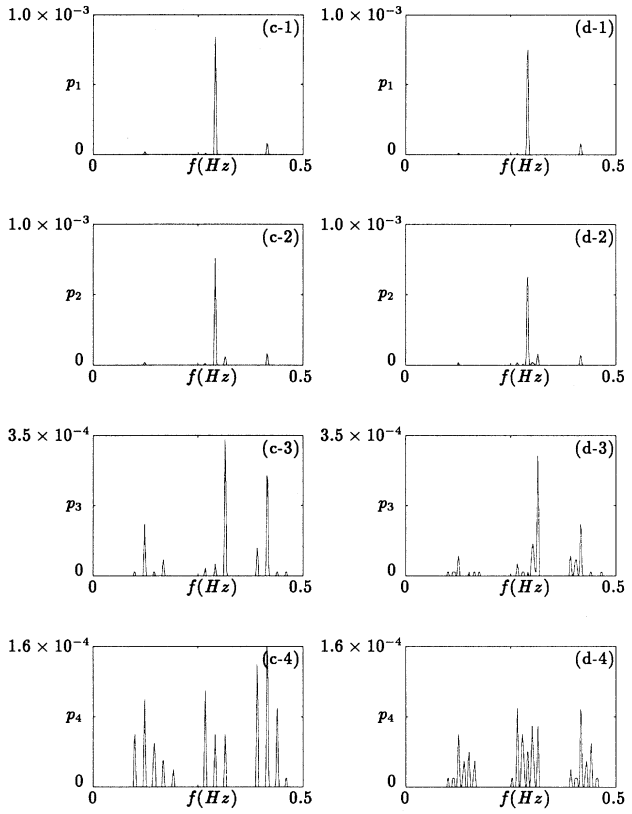

FIG. 7. Power spectra for time-varying amplitudes (chronos) 1–4. The letters "c" and "d" in parentheses at the top right corner of each plot refer to the 1-torus [Fig. 3(a)] and chaotic attractor [Fig. 3(f)], respectively, while the number denotes the corresponding mode. The horizontal axes denote the frequency in Hz while the vertical axes represent the power. Initial condition A is used.

TABLE II. Effect of zero mean white noise on the energy content of the less dominant modes of the chaotic attractor ($L = 1.43$).

	Singular values with noise variance of				
Mode	0.0	0.001	0.01	0.1	1.0
1	48.34	48.91	48.96	49.48	54.43
2	18.24	18.48	18.59	19.70	28.67
3	8.72	8.82	9.16	11.78	26.96
4	5.64	5.73	6.13	9.30	26.40
5	3.45	3.56	4.20	8.54	25.96
6	2.17	2.24	3.00	8.12	24.77
7	1.24	1.48	2.76	7.93	24.48
8	0.81	1.10	2.63	7.81	24.08
9	0.45	0.871	2.58	7.70	23.46
10	0.33	0.868	2.399	7.50	22.90
11	0.19	0.78	2.396	7.34	22.82
12	0.13	0.76	2.35	7.23	22.53
13	0.08	0.75	2.30	7.13	21.82
14	0.05	0.73	2.24	6.79	20.94
15	0.04	0.70	2.17	6.68	20.81
16	0.024	0.69	2.09	6.55	20.34
17	0.013	0.66	2.05	6.39	19.86
18	0.008	0.65	2.00	6.24	19.43
19	0.002	0.64	1.97	6.10	19.21

distorted. Increasing contributions of the lower energy modes (3 to 19) which are in general more disordered provided a quantitative measure of the effect of noise as is illustrated in Table II.

IV. EXTERNAL FORCING

The existence of a dominant frequency in the first mode would pose the question: Can one obtain quasiperiodic and periodic behavior from chaos by harmonically forcing the system at the dominant frequency? Thus before proceeding to develop a suitable feedback control framework, an attempt is made in this section to study the system response to harmonic (sinusoidal) forcing functions applied to either the boundary conditions or the differential equation with a view to identifying regions in parameter space that could display quasiperiodic or periodic behavior. The adjustable parameters include amplitude, frequency, and possibly wave number. A systematic study of the behavior of the system as a function of these parameters is equivalent to construction of a resonance diagram containing Arnold's tongues which would require large computational effort. However, the emphasis here is to illustrate with specific examples that the system, if suitably forced, could indeed demonstrate periodic and quasiperiodic behavior. Instead of extensively searching the parameter space, one could utilize the dynamic information obtained from the singular value decomposition of the spatiotemporal data in choosing the values for frequency and wave number. For example, a frequency interval of 0.2 to 0.4 Hz was chosen based on the information from the power spectra (Fig. 7). The topos (Fig. 5) and the distribution of energy among the various modes suggested π to 4π to be a resonable interval for the wave number. A degree of freedom existed with regard to amplitudes. Here they were chosen keeping in mind that chaos (in LPS) had been shown to be controllable by small amplitude parametric perturbations. This procedure in no way eliminates the possibility of the existence of periodicity and quasiperiodicity in some other regions of parameter space.

Two kinds of forcing functions were used — one that harmonically varied the boundary conditions at $z = 0$ in Eqs. (9) and (10):

$$X_0 = \bar{X} + a\sin(2\pi f t), \tag{14}$$

$$Y_0 = \bar{Y} + a\sin(2\pi f t), \tag{15}$$

and the other that varied B in the system of ODEs [Eqs. (7) and (8)]:

$$B = \tilde{B} + a\sin(\kappa z - 2\pi f t), \tag{16}$$

where a is the amplitude, f is the frequency, κ is the wave number, and $\tilde{B}$ is 5.45.

The rich nonlinear dynamics of the unforced system indicated that a wide range of attractors would be observed when the system is forced externally. This was indeed the case as seen from a number of simulations. The examples presented here correspond to instances when consis-

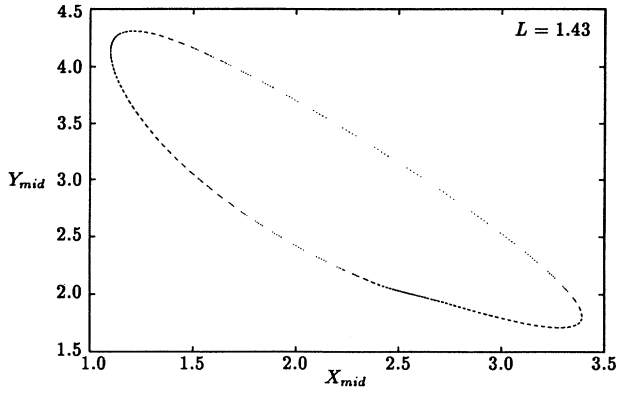

FIG. 8. Quasiperiodic behavior from boundary forcing of the chaotic attractor [Fig. 3(f)]. The forcing function is of the form described by Eqs. (14) and (15) with unit amplitude and a period of 3.1 sec.

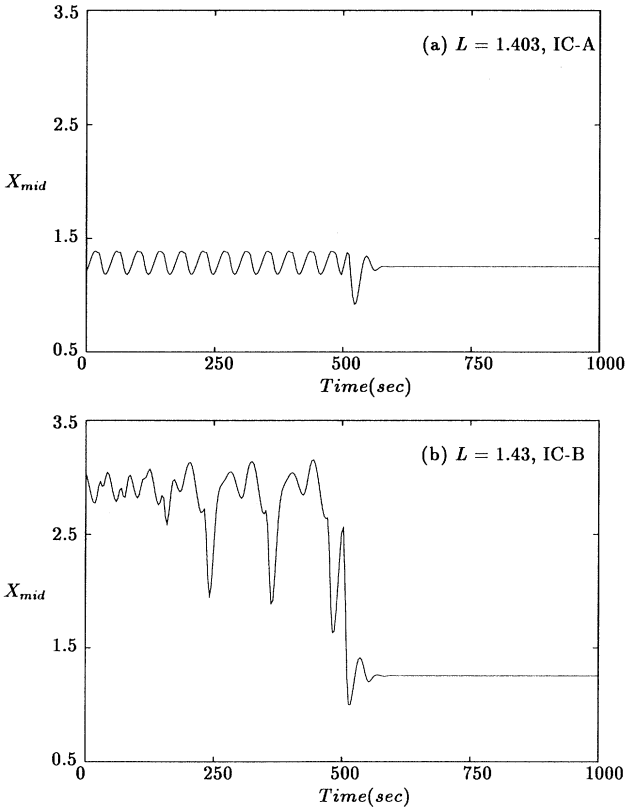

FIG. 9. Periodic attractor resulting from spatiotemporal forcing of B. The forcing function [Eq. (16)] is characterized by an amplitude of 0.05, wave number of π, and frequency of 0.3 Hz. The first 500 sec represent either (a) the behavior of the torus using initial condition A [Fig. 3(a)] or (b) the chaotic attractor using initial condition B [Fig. 3(f)] after which the forcing function is activated.

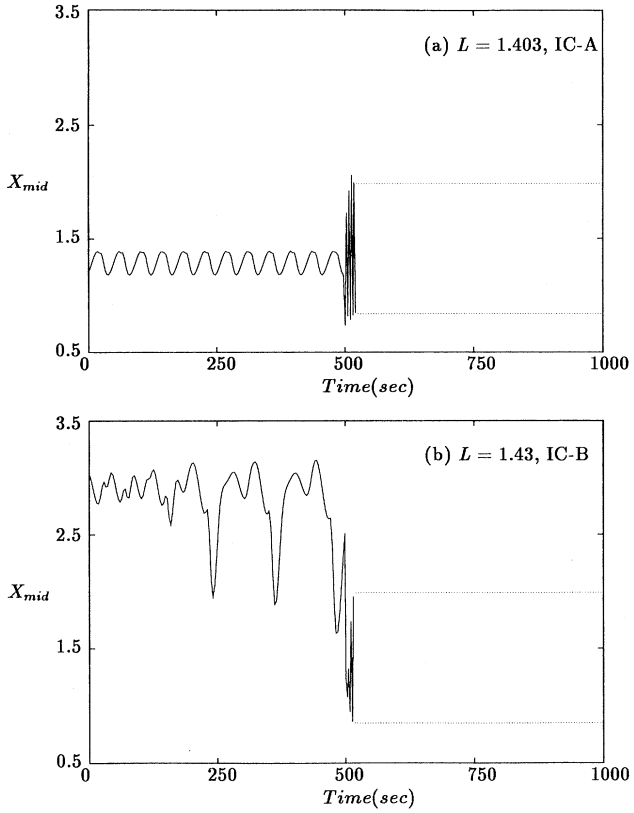

FIG. 10. Period-doubling effect due to spatiotemporal forcing of B. The forcing function [Eq. (16)] is characterized by unit amplitude, a wave number of π, and frequency of 0.4 Hz. The first 500 sec represent either (a) the behavior of the torus using initial condition A [Fig. 3(a)] or (b) the chaotic attractor using initial condition B [Fig. 3(f)] after which the forcing function is activated.

tent periodic or quasiperiodic behavior was obtained not just for the chaotic attractor but for the entire transition regime.

A quasiperiodic attractor (Fig. 8) was obtained when the chaotic system was forced at the boundary with unit amplitude and a period (reciprocal of frequency) of 3.1 sec. The Poincaré map shown in Fig. 8 corresponds to $L = 1.43$ but a near identical attractor was obtained for other values of L spanning the complete transition regime, i.e., L =1.403 to 1.43. Thus chaos has been totally eliminated in this region. Spatiotemporal forcing of B as in Eq. (16) yielded periodic behavior for an amplitude of 0.05, frequency of 0.3 Hz, and wave number of π. This is illustrated in Fig. 9, which represents the concentration of X at the midpoint of the reactor (corresponding to the profiles which lie on the Poincaré map) as a function of time. The initial 500 sec correspond either to the behavior of the torus or chaotic attractor before the forcing function is activated. Period-doubling behavior was observed as shown in Fig. 10 when B was forced with unit amplitude, frequency of 0.4 Hz, and wave number of π.

V. MODAL FEEDBACK CONTROL

The primary goal is to develop a feedback control framework which would facilitate control in the transition region. The objective could be control of the chaotic attractor to any of the tori from which it evolves or vice versa or from one torus to another. Kittel *et al.* [30] demonstrated by the use of small feedback perturbations that it was indeed possible to transform the unpredictable chaotic behavior into a predictable chaotic or periodic motion via stabilization of unstable, aperiodic, or periodic orbits of the strange attractor. This method was primarily based on the idea of driving systems with chaotic or aperiodic signals introduced by Pecora and Carroll [27,28] and briefly described in Sec. II. If the aim is to control the chaotic attractor to the torus then the system with chaotic behavior corresponds to the *response* subsystem [Eqs. (1) and (2) with $L = 1.43$] and the system whose dynamics are characterized by one of the tori corresponds to the *drive* subsystem [for example, Eqs. (1) and (2) with $L = 1.403$] in the terminology of Pecora and Carroll. One could alternatively view this in the conventional feedback control framework where the dynamic behavior of the *drive* and *response* subsystems correspond to the *set point* and *output*, respectively. The *drive* influences the *response* through the control action which depends on the deviation of the *output* from the *set point*.

The approach of Pecora and Carroll is applicable to a system of any dimension. If translated directly to the context of DPS [Eqs. (1) and (2)], an infinite number of controllers would be needed. Such an implementation treats the DPS as a high-dimensional LPS and hence fails to utilize the spatial information. The theory of DPS suggests that although the dimension of the system may be infinity, there may exist only a few dominant modes. It is conceivable then that identifying the dominant modes would help reduce the dimension of the system without sacrificing much information. The control strategy could then be designed by considering only these dominant modes. Identification and control of these modes may be accomplished by means of the singular value decomposition as demonstrated in [32,33]. A modal feedback control methodology that accounts for the spatial nature of the output is schematically depicted in Fig. 11.

A detailed discussion of modal control can be found in [52]. First, let us suppose that we wish to control the chaotic attractor to the 1-torus. Let $X(z,t)$ in the open loop represent chaotic behavior and $X_{SP}(z,t)$ be indicative of the desired quasiperiodic behavior. Thus the set point is a dynamically varying profile. $\varepsilon(z,t)$ is the deviation of the output profile $X(z,t)$ from the set point $X_{SP}(z,t)$:

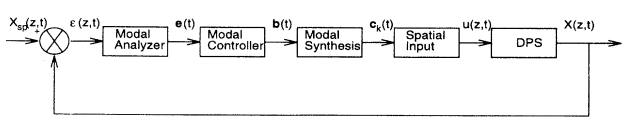

FIG. 11. Modal feedback control scheme.

$$\varepsilon(z,t) = X_{SP}(z,t) - X(z,t). \tag{17}$$

Since the topos $w_i(z)$ were shown to be intrinsic properties of the system (i.e., consistent throughout the transition regime), the modal error vector $\mathbf{e}(t)$ is obtained by projecting the deviation $\varepsilon(z,t)$ onto the topos:

$$e_i(t) = \int_0^1 \varepsilon(z,t) w_i(z)\, dz. \tag{18}$$

The modal controller computes the control coefficients $b_i(t)$ corresponding to each $e_i(t)$. A suitable form of control law could be used. For instance, with proportional control,

$$b_i(t) = K e_i(t). \tag{19}$$

The control action $u(z,t)$ is then obtained as follows:

$$u(z,t) = \sum_{i=1}^{N} b_i(t) w_i(z). \tag{20}$$

Though a distributed parameter system is of infinite dimension (i.e., $N = \infty$), in practice N could be set to a value which ensures that the first N modes capture the desired amount (for example, 90%) of the original behavior. This information can be obtained from the singular values. It is difficult to practically implement a control action of the type described by Eq. (20) that is continuous in space. A more physically realizable technique would be having M zones of piecewise uniform control in the interval $z_k < z < z_{k+1}$ (cf. Fig. 1 for an example). The control action could then be expressed as

$$u(z,t) = \sum_{k=1}^{M} c_k(t) g_k(z), \tag{21}$$

where

$$g_k(z) = H(z - z_k) - H(z - z_{k+1}). \tag{22}$$

$H(z)$ refers to the Heaviside step function. $c_k(t)$ can be obtained by using the orthogonality of $g_k(z)$:

$$c_k(t) = \sum_{i=1}^{N} b_i(t) \int_0^1 w_i(z) g_k(z)\, dz. \tag{23}$$

Control of the type described by Eq. (21) could be classified as *spatial control* since it is applied across the entire spatial domain. There may be instances when it might be possible to exert the control only at the boundary (inlet) and these cases correspond to *boundary control*. Here, the control u is a function only of time. A possible candidate for the control law is one which drives the instantaneous integral cubed deviation defined as

$$\epsilon(t) = \int_0^1 [X_{SP}(z,t) - X(z,t)]^3\, dz \tag{24}$$

toward zero. The cubic is used because a square law would yield only positive control actions while the unit power would lead to positive and negative area cancellation. Any suitable design can be used for the resultant

controller which is functionally expressed as

$$u(t) = g(\epsilon(t)). \tag{25}$$

In the reaction-diffusion system [Eqs. (1) and (2)] *spatial control* is physically accomplished by the addition or removal of reactants A and B as shown in Fig. 1. Thus we have a multivariable system with two inputs (A and B) and two outputs (X and Y). The control strategy here involves designing two independent single-loop controllers with each controller using a single input to control a selected output. The input-output pairing (A-X and B-Y) is ascertained by calculating the relative gain array (RGA) [53] for the set of ordinary differential equations obtained by projecting the set of closed loop equations (28) and (29) onto the first topos for X and Y, respectively. In order to obtain the pairing using the relative gain array, the resultant equations are linearized around the steady state ($X = 2$, $Y = 2.725$, $A = 2$, $B = 5.45$) to obtain the proper Jacobian. Only a single mode is retained in the calculations since it contains nearly 85% of the total energy.

The exact increments or decrements of A and B, referred to as u_X and u_Y, are computed based on the deviations of $X(z,t)$ and $Y(z,t)$ from $X_{SP}(z,t)$ and $Y_{SP}(z,t)$, respectively. Equations (17)–(19), and (23) can be combined with Eq. (21) to yield the following expression for u_X:

$$u_X(z,t) = \sum_{k=1}^{M}\sum_{i=1}^{N} K\left(\int_0^1 [X_{SP}(z',t) - X(z',t)] \times w_i(z')\,dz'\right) \times \left(\int_0^1 w_i(z')g_k(z')\,dz'\right) g_k(z), \tag{26}$$

where K is the proportional gain. The analogous expression for u_Y is

$$u_Y(z,t) = \sum_{k=1}^{M}\sum_{i=1}^{N} K\left(\int_0^1 [Y_{SP}(z',t) - Y(z',t)] \times w_i(z')\,dz'\right) \times \left(\int_0^1 w_i(z')g_k(z')\,dz'\right) g_k(z). \tag{27}$$

The same symbol $w_i(z)$ is used for the topos corresponding to X and Y since they were found to be nearly identical for both cases. Proportional feedback is used based on the observation that earlier works dealing with the problem of control of chaos have found such a scheme adequate for the purpose of stabilization of the strange attractor onto one of the embedded unstable orbits. With the inclusion of feedback control the governing equations (1) and (2) are transformed to

$$\frac{\partial X}{\partial t} = \frac{D_X}{L^2}\frac{\partial^2 X}{\partial z^2} + X^2Y - (B + u_Y + 1)X + (A + u_X), \tag{28}$$

$$\frac{\partial Y}{\partial t} = \frac{D_Y}{L^2}\frac{\partial^2 Y}{\partial z^2} - X^2Y + (B + u_Y)X. \tag{29}$$

The boundary conditions [Eqs. (3) and (4)] remain unchanged. A potential complication though is the coupling of the control action u_Y with the concentration of X. Earlier works in the area of control of chaos to aperiodic trajectories [29,30] were restricted to cases where the control action appeared linearly in the equations. Also, Gay and Ray [32,33] and Chen and Chang [34] addressed problems in distributed systems where the control term was not directly coupled with any of the output variables.

The approach here is to try several forms of modal control. As in the case of dynamics, the computations are performed using the finite difference approximation with 20 intervals of equal length. The corresponding set of ODEs is

$$\frac{dX_i}{dt} = \frac{D_X}{L^2h^2}(X_{i-1} - 2X_i + X_{i+1}) + X_i^2Y_i - (B + u_{Y_i} + 1)X_i + (A + u_{X_i}), \tag{30}$$

$$\frac{dY_i}{dt} = \frac{D_Y}{L^2h^2}(Y_{i-1} - 2Y_i + Y_{i+1}) - X_i^2Y_i + (B + u_{Y_i})X_i, \tag{31}$$

where i varies from 1 to 19. As shown above, the SVD analysis would produce 19 modes for this system and in principle one could use all 19 modes when computing u_X and u_Y. However, the distribution of the singular values (Table I) indicates that nearly 85% of the energy is concentrated in the first mode itself. Hence, control is performed using the first mode alone so that $N = 1$. Also, only one zone is used, i.e., $M = 1$ so that the control action is spatially uniform across the entire length of the reactor. Equation (26) simplifies to

$$u_X(z,t) = K\left(\int_0^1 [X_{SP}(z,t) - X(z,t)]\,w_1(z)\,dz\right) \times \left(\int_0^1 w_1(z)g_1(z)\,dz\right) g_1(z). \tag{32}$$

Note that $g_1(z)$ is unity in the above equation and hence, is not explicitly mentioned in the equations to follow. For simplicity, the integral $\int_0^1 w_1(z)\,dz$ is combined with the proportional gain K so that the performance of the control scheme is studied using the following expression:

$$u_X(z,t) = K_1\left(\int_0^1 [X_{SP}(z,t) - X(z,t)]\,w_1(z)\,dz\right) \tag{33}$$

and an analogous one for u_Y:

$$u_Y(z,t) = K_1\left(\int_0^1 [Y_{SP}(z,t) - Y(z,t)]\,w_1(z)\,dz\right). \tag{34}$$

Identical values of K_1 are used for both u_X and u_Y. Also Eqs. (33) and (34) are modified to the appropriate inner products between the deviation vector and the first topos when applying them to Eqs. (30) and (31). Use of a single zone would also imply that u_{X_i} and u_{Y_i} are identical for all i.

Careful inspection of the dynamics (Sec. III) revealed the existence of two distinct torus-doubling routes to

chaos (Fig. 3). However, for each value of the bifurcation parameter L, the asymmetric attractors in the two sequences were coexisting and mirror symmetric. This was demonstrated by the use of mirror-symmetric initial conditions. A possible implication of this would be that one would have to perform two sets of simulations to study the effects of the control strategy on the two coexisting chaotic attractors. Fortunately, the existence of the left-right, i.e., $(z, 1-z)$ symmetry (as demonstrated by SVD and Poincaré maps using different surfaces) ensured that by simultaneously generating the Poincaré maps for both surfaces $X_{z=\zeta}(t) = 2.0$ and $X_{z=1-\zeta}(t) = 2.0$, the control of both mirror-symmetric chaotic attractors could be achieved with a single simulation.

Figure 12 compares the original 1-torus [Fig. 3(a)] to the one obtained by controlling the chaotic attractor [Fig. 3(f)] using only the most dominant mode $\mathbf{w_1}(z)$ with $K_1 = 0.03$. Clearly, the control strategy brings the chaotic attractor to a torus close to the "set point" torus. The results of attempting to direct the chaotic attractor to a 2-torus are displayed in Fig. 13.

If we wished to consider 19 zones of control action possible (see Fig. 1), then we could define a new variable u_Y' as the original one in Eq. (27) divided by the concentration X at each zone, i.e., $u_Y' = u_Y/X$. In this case u_Y appears linearly in the equation. This can be implemented in a relatively straightforward manner for the general case of M zones of piecewise uniform control [Eq. (21)] by scaling the proposed control move corresponding to each zone with the reciprocal of the concentration of X within that zone.

$$u(z,t) = \sum_{k=1}^{M} \frac{c_k(t) g_k(z)}{X_{z_0}}, \quad \text{where } z_k \le z_0 \le z_{k+1}. \tag{35}$$

The concentration X_{z_0} could potentially correspond to the value measured by a single sensor in the zone or to an average if more than one sensor is used in a single zone.

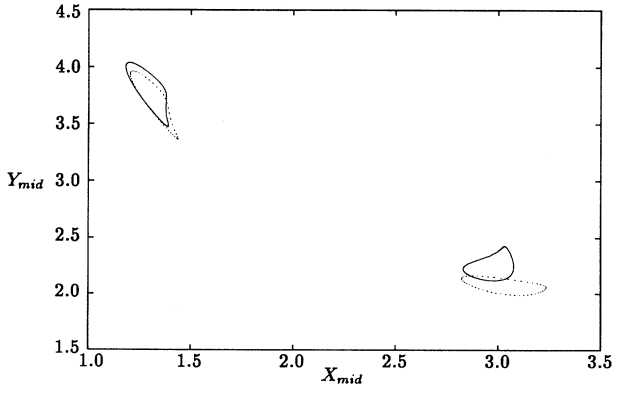

FIG. 12. Poincaré map depicting the control of the open loop chaotic attractor [Fig. 3(f)] to the underlying 1-torus using a single zone and the most dominant mode. Equation (11) defines the Poincaré surface. $K_1 = 0.03$, solid line refers to the "set point" attractor, dots refer to the controlled attractor.

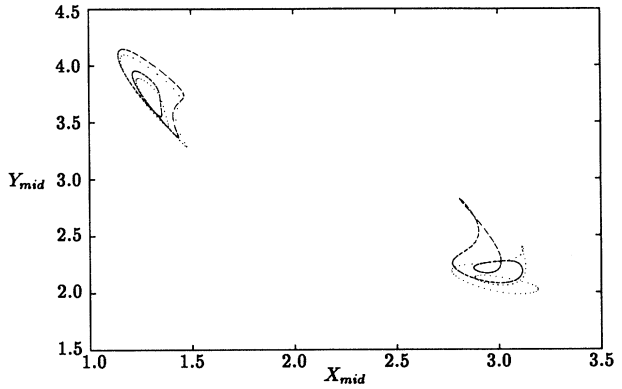

FIG. 13. Poincaré map depicting the control of the open loop chaotic attractor [Fig. 3(f)] to the underlying 2-torus using a single zone and the most dominant mode. Equation (11) defines the Poincaré surface. $K_1 = 0.03$, solid line refers to the "set point" attractor, dots refer to the controlled attractor.

As a preliminary investigation, rather than using the complete freedom of M zones, u_Y' is chosen as

$$u_Y' = c(t) \sum_{k=1}^{M} \frac{g_k(z)}{X_{z_0}}, \quad \text{where } z_k \le z_0 \le z_{k+1}, \tag{36}$$

where $c(t)$ does not depend on k, i.e., the incremental amount of B [Eq. (34)] is scaled by the reciprocal of the concentration of X at each of the 19 locations. The incremental amount of A to be added [Eq. (33)] can also be scaled $u_X' = u_X - u_Y'$. In this case,

$$\frac{dX_i}{dt} = \frac{D_X}{L^2h^2}(X_{i-1} - 2X_i + X_{i+1}) + X_i^2 Y_i - (B+1)X_i + A + u_X, \tag{37}$$

$$\frac{dY_i}{dt} = \frac{D_Y}{L^2h^2}(Y_{i-1} - 2Y_i + Y_{i+1}) - X_i^2 Y_i + BX_i + u_Y. \tag{38}$$

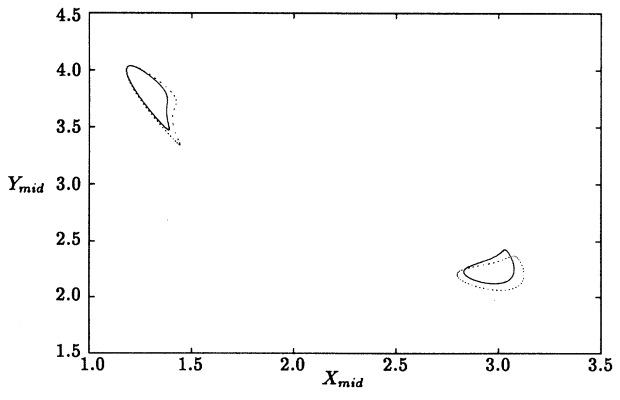

FIG. 14. Poincaré map depicting the control of the open loop chaotic attractor [Fig. 3(f)] to the underlying 1-torus using 19 zones and the most dominant mode. Equation (11) defines the Poincaré surface. $K_1 = 0.03$, solid line refers to the "set point" attractor, dots refer to the controlled attractor.

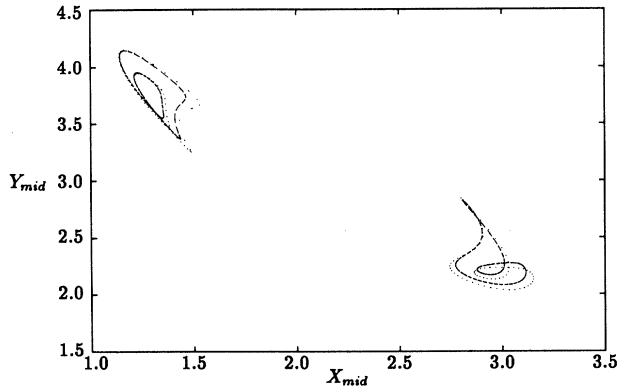

FIG. 15. Poincaré map depicting the control of the open loop chaotic attractor [Fig. 3(f)] to the underlying 2-torus using 19 zones and the most dominant mode. Equation (11) defines the Poincaré surface. $K_1 = 0.03$, solid line refers to the "set point" attractor, dots refer to the controlled attractor.

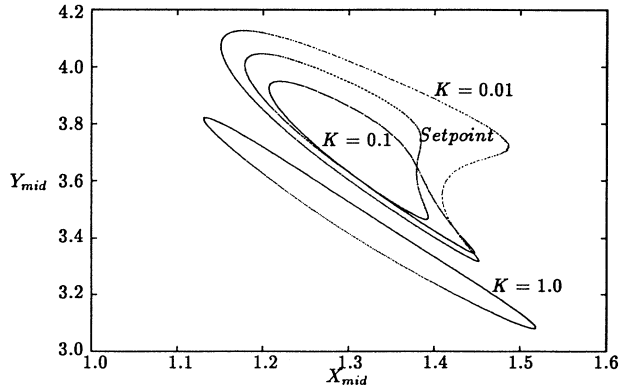

FIG. 17. Poincaré map depicting the control of the open loop chaotic attractor [Fig. 3(f)] to the underlying 1-torus as a function of the proportional gain K. Nineteen zones and the most dominant mode are used. Equation (11) defines the Poincaré surface.

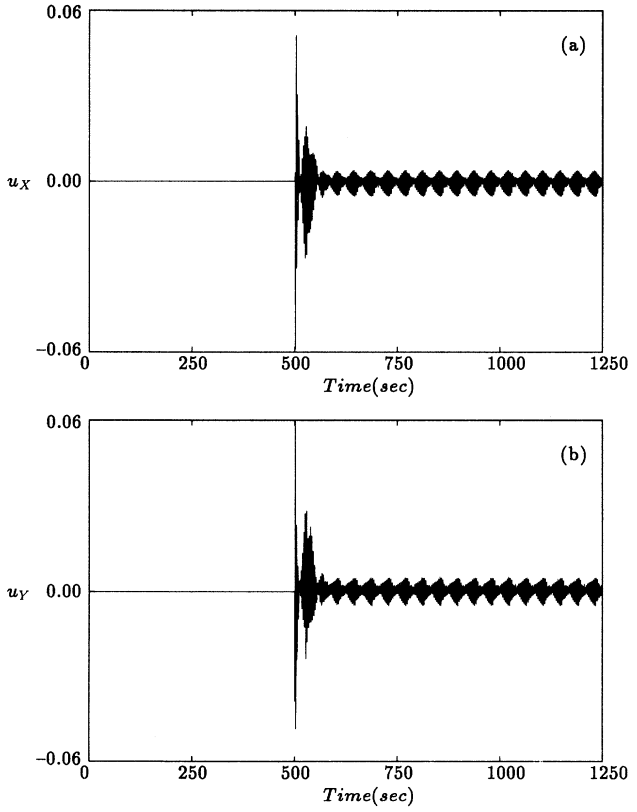

FIG. 16. Sequence of control moves when directing the open loop chaotic attractor to the underlying 1-torus using 19 zones and the most dominant mode (Fig. 14). $K_1 = 0.03$. The vertical axes in (a) and (b) correspond to the control moves u_X and u_Y [Eqs. (33) and (34)] which refer to the additional amounts of A and B to be added or removed along the sides of the reactor. Control is activated after 500 seconds.

Figures 14 and 15 illustrate the results of trying to direct the chaotic attractor [cf. Fig. 3(f)] to the 1- and 2-torus, respectively, with $K_1 = 0.03$. The resulting attractors though not in exact agreement with the desired tori do show a greater resemblance in terms of shape, location, and orientation as compared to the attractors in Figs. 12 and 13. Thus allowing u'_X and u'_Y to depend on spatial location, z, expectedly enhances the performance of the control strategy. The scaled control moves u_X and u_Y, when bringing the chaotic attractor to the 1-torus, settle down to a periodic sequence rather small in magnitude as compared to the initial steps as shown in Fig. 16. Note that the control is applied only after 500 sec.

Figure 17, which represents the tori that result for different values of K, indicates that the choice of proportional gain needs to be made based on the fact that a very small value may not alter the original behavior of

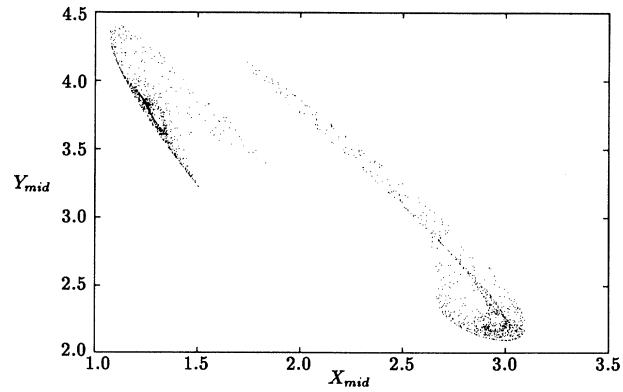

FIG. 18. Poincaré map depicting the control of the open loop 1-torus [Fig. 3(a)] to the chaotic attractor using 19 zones and the most dominant mode. Equation (11) defines the Poincaré surface. $K_1 = 0.03$. Refer to Fig. 3(f) for the "set point" attractor.

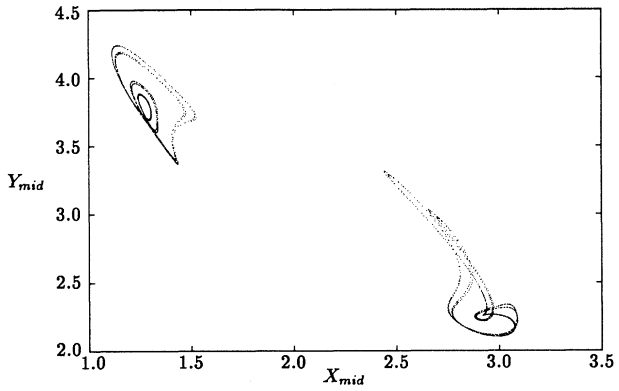

FIG. 19. Poincaré map depicting the control of the open loop 1-torus [Fig. 3(a)] to the 8-torus using 19 zones and the most dominant mode. Equation (11) defines the Poincaré surface. $K_1 = 0.03$. Refer to Fig. 3(e) for the "set point" attractor.

the system and a very large value may drive the system away from the set point, i.e., desired behavior.

This control methodology is general in the sense that with very subtle control moves one can stabilize the chaotic attractor to any higher torus by appropriately modifying the set point. There are instances when it might be desirable to introduce chaotic behavior. In the current framework this can be achieved by suitably choosing the set point to represent the chaotic behavior and the open loop behavior of the system to correspond to any of the tori. An example of directing the 1-torus [Fig. 3(a)] to the chaotic attractor [Fig. 3(f)] is presented in Fig. 18. For the sake of clarity only the controlled attractors are presented [see Fig. 3(f) for the "set point" chaotic attractors]. The same procedure can also be used to obtain any torus from any other torus. For instance, it is possible to control the 1-torus [Fig. 3(a)] to the 8-torus [Fig. 3(d)] as shown in Fig. 19.

One could alternately treat the above control problem

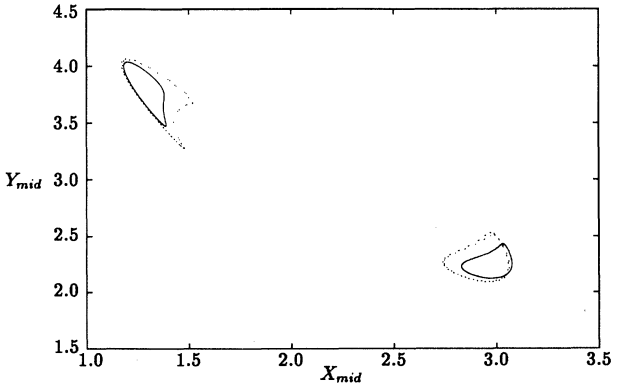

FIG. 20. Poincaré map depicting the boundary control of the open loop chaotic attractor [Fig. 3(f)] to the underlying 1-torus using the most dominant mode. Equation (11) defines the Poincaré surface. $K = 1.0$, solid line refers to the "set point" attractor, dots refer to the controlled attractor.

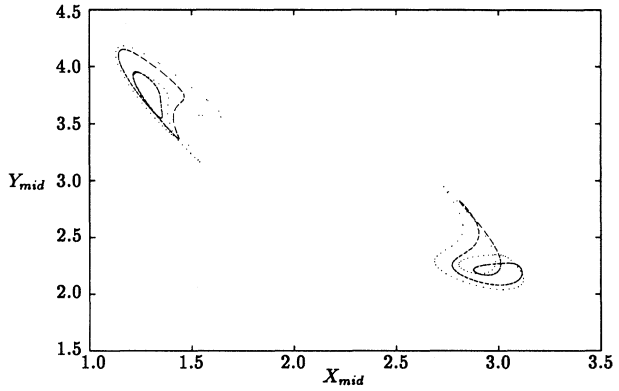

FIG. 21. Poincaré map depicting the boundary control of the open loop chaotic attractor [Fig. 3(f)] to the underlying 2-torus using the most dominant mode. Equation (11) defines the Poincaré surface. $K = 1.0$, solid line refers to the "set point" attractor, dots refer to the controlled attractor.

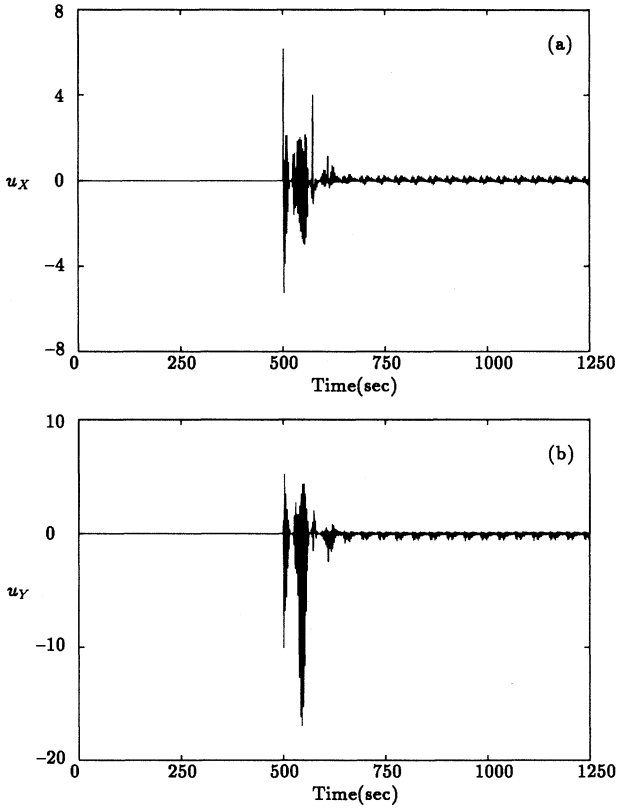

FIG. 22. Sequence of boundary control moves when directing the open loop chaotic attractor to the underlying 1-torus using the most dominant mode (Fig. 20). A proportional gain of 1.0 is used. The vertical axes in (a) and (b) correspond to the control moves u_X and u_Y [Eqs. (41) and (42)] which refer to the additional amounts of X and Y to be added or removed at the inlet of the reactor. Control is activated after 500 sec.

from the perspective of a high-dimensional multivariable lumped parameter system. Here, the control moves (increments or decrements of A and B) are calculated by comparing the concentrations of X and Y as measured by the sensors along the length of the membrane reactor in Fig. 1 to the desired values at each of those specific locations. A distinct control move is associated with each location. Such an approach, when applied to the problem of directing the chaotic attractor [Fig. 3(f)] to the 1-torus [Fig. 3(a)], succeeds in eliminating the chaotic behavior but the resultant quasiperiodic behavior is not close to the desired one.

Another possible approach could be to use a control that seeks to minimize the integral of the deviation of the output profile from the set point profile (i.e., $\int_0^1 [X_{SP}(z,t) - X(z,t)]\, dz$). This approach also eliminates the chaotic behavior but fails to yield the desired quasiperiodic behavior. Furthermore, the control moves are an order of magnitude higher than the ones observed in Fig. 16. The modal approach which uses a knowledge of the system structure is much more effective.

Boundary control is implemented by suitably modifying only the boundary conditions at the inlet, i.e., changing the concentrations of X and Y at $z = 0$:

$$X(t,0) = \bar{X} + u_X(t), \tag{39}$$

$$Y(t,0) = \bar{Y} + u_Y(t). \tag{40}$$

Again a single mode is used. In this case, the control law [cf. Eqs. (24) and (25)] is reducible to the form:

$$u_X(t) = K \left(\int_0^1 [X_{SP}(z,t) - X(z,t)]\, w_1(z)\, dz \right)^3, \tag{41}$$

$$u_Y(t) = K \left(\int_0^1 [Y_{SP}(z,t) - Y(z,t)]\, w_1(z)\, dz \right)^3. \tag{42}$$

Examples of the stabilization of the chaotic attractor to 1-torus and 2-torus are shown in Figs. 20 and 21. The sequences of control moves u_X and u_Y when stabilizing the 1-torus are presented in Fig. 22. The proportional gain needs to be much larger than the one used for spatial control. Intuitively this is to be expected as one is trying to influence the behavior of the entire spatial domain from one end in boundary control rather than from the entire spatial domain itself as in spatial control. It is interesting to note that this effect manifested itself also in terms of the amplitude required to generate quasiperiodicity or periodicity when forcing the system externally.

VI. CONCLUSIONS

Through properly chosen Poincaré maps, it was observed that the dynamics of the reaction-diffusion system with Brusselator kinetics (in the parameter space of interest $L = 1.403$ to 1.43) is characterized by the presence of two coexisting and mutually mirror symmetric spatially asymmetric attractors which show different sensitivities to noise at different spatial locations. The mirror-symmetry was initially ascertained from the use of mirror-symmetric sets of initial conditions.

This finding was also corroborated from the relationship between the topos for the two sequences of attractors. Thus singular value decomposition proved to be a useful tool in detecting the presence of coexisting and mutually mirror-symmetric attractors. The consistency of the topos throughout the transition region coupled with the distribution of energy among the various modes suggested their possible use in the development of the control strategy. The power spectra of the chronos captured the effect of the onset of chaos and also identified the dominant frequencies. It was shown that the system if suitably forced externally could exhibit periodic or quasiperiodic behavior.

Finally a modal control strategy was developed and applied to the control of chaos occurring through the torus-doubling route in the reaction-diffusion system. The key idea was to compute the control action by projecting the deviation of the current dynamic behavior of the system from the desired behavior onto the dominant modes. Spatial and boundary implementations of the control scheme were tested. As one would expect, using more zones for control was found to enhance the performance of the control scheme. It was possible, with very subtle control action, to obtain behavior close to any of the tori by suitably controlling the chaotic attractor and vice versa. Although applied to an example which demonstrated a quasiperiodic route to chaos, the control scheme is essentially independent of the route to chaos and so could potentially be applied to instances of chaos in distributed parameter systems occurring through other routes too.

The control strategy that has been described relies on the ordering of the modes remaining consistent at all time scales. However, for instances of the flow being driven by events that dominate over very short time scales, such as homoclinic or heteroclinic bursts, the procedure would need to be modified. The papers by Kirby and Armbruster [45] and Graham and Kevrekidis [54] address this issue.

ACKNOWLEDGMENTS

The authors gratefully acknowledge the support provided by the U.S. Department of Energy. Also, we are indebted to the O. A. Hougen Fund, University of Wisconsin–Madison, for providing financial support for M. M.

APPENDIX: DETAILS OF THE APPLICATION OF SINGULAR VALUE DECOMPOSITION TO SPATIOTEMPORAL DATA

The spatiotemporal data for reactant X typically consist of M snapshots at N points in space which constitutes an $N \times M$ matrix $\mathbf{X}'$. Thus the N rows represent the spatial coordinate while the M columns correspond to the time coordinate. In this work, $N < M$. The jkth

element of $\mathbf{X}'$, also expressed as $x'(z_j, t_k)$, denotes the concentration of X at the jth spatial location z_j and kth time instant t_k. For convenience the subscripts j, l are used for the spatial coordinate while k, m apply to the time coordinate. Hence j, l range from 1 to N while k, m range from 1 to M.

The first step involves separating $\mathbf{X}'$ into a time-averaged part $\bar{\mathbf{X}}$ and time-varying part $\mathbf{X}$ as follows:

$$\mathbf{X}' = \bar{\mathbf{X}} + \mathbf{X}, \tag{A1}$$

where the jkth element of $\bar{\mathbf{X}}$ is

$$\bar{x}(z_j, t_k) = \frac{1}{M} \sum_{m=1}^{M} x'(z_j, t_m) = \bar{x}(z_j). \tag{A2}$$

By construction, $\bar{\mathbf{X}}$ simply consists of M identical columns, thus rendering the time suffix redundant.

SVD is then performed only on the time-varying part $\mathbf{X}$ to yield

$$\mathbf{X} = \mathbf{W}\Sigma\mathbf{V}^*, \tag{A3}$$

where $\mathbf{W}$ and $\mathbf{V}$ are unitary matrices of order $N \times N$ and $M \times M$, respectively, such that

$$\Sigma = \mathbf{W}^*\mathbf{X}\mathbf{V} = \mathrm{diag}(\sigma_1, ..., \sigma_p), \quad p = \min[N, M] = N,$$

where

$$\sigma_1 \geq \sigma_2 \geq \cdots \geq \sigma_p \geq 0.$$

Σ is referred to as the singular value matrix of $\mathbf{X}$ and the diagonal entries are the singular values. $\mathbf{W}$ and $\mathbf{V}$ are the left and right singular matrices, respectively. Associated with each of the singular values σ_i in Σ are the ith column of $\mathbf{W}$, denoted as $\mathbf{w}_i$, and the ith column of $\mathbf{V}$, denoted as $\mathbf{v}_i$, which are termed the ith left and right singular vectors, respectively. Thus the columns of $\mathbf{W}$ and $\mathbf{V}$ are the left (spatially dependent) and right (time-dependent) singular vectors. The jith element of $\mathbf{W}$, $\mathbf{w}_i(z_j)$, represents the value of the ith left singular vector $\mathbf{w}_i$ at the jth spatial location z_j. The kith element of $\mathbf{V}$, $\mathbf{v}_i(t_k)$, represents the value of the ith right singular vector $\mathbf{v}_i$ at the kth time instant t_k. The singular values and vectors satisfy the following properties for $i = 1, N$:

$$\sum_{l=1}^{N} \sum_{k=1}^{M} x(z_j, t_k) x(z_l, t_k) w_i(z_l) = \sigma_i^2 w_i(z_j), \tag{A4}$$

$$\sum_{j=1}^{N} x(z_j, t_k) w_i(z_j) = \sigma_i v_i(t_k), \tag{A5}$$

$$\sum_{m=1}^{M} \sum_{j=1}^{N} x(z_j, t_k) x(z_j, t_m) v_i(t_m) = \sigma_i^2 v_i(t_m), \tag{A6}$$

$$\sum_{k=1}^{M} x(z_j, t_k) v_i(t_k) = \sigma_i w_i(z_j), \tag{A7}$$

which could be expressed in more compact form as

$$\mathbf{X}\mathbf{X}^*\mathbf{w}_i = \sigma_i^2 \mathbf{w}_i, \tag{A8}$$

$$\mathbf{X}^*\mathbf{w}_i = \sigma_i \mathbf{v}_i, \tag{A9}$$

$$\mathbf{X}^*\mathbf{X}\mathbf{v}_i = \sigma_i^2 \mathbf{v}_i, \tag{A10}$$

$$\mathbf{X}\mathbf{v}_i = \sigma_i \mathbf{w}_i. \tag{A11}$$

In the above form, the matrix SVD resembles the corresponding relations for the more general singular value decomposition of a function of two variables. For example, if $\mathbf{X}(z, t)$ was a continuous function of z and t rather than a discrete data set, it could be expanded as

$$\mathbf{X}(z, t) = \sum_{n=1}^{\infty} \mathbf{w}_n(z) \sigma_n \bar{\mathbf{v}}_n(t), \tag{A12}$$

where $\mathbf{w}_n$ and $\mathbf{v}_n$ are the nth left and right singular functions. The overbar denotes the complex conjugate and σ represents the singular values.

Thus the singular values are the positive square roots of the eigenvalues of the Hermitian matrices $\mathbf{X}\mathbf{X}^*$ and $\mathbf{X}^*\mathbf{X}$ and hence unique. The left singular vectors $\mathbf{w}_i$ are the eigenvectors of $\mathbf{X}\mathbf{X}^*$ while the right singular vectors $\mathbf{v}_i$ are the eigenvectors of $\mathbf{X}^*\mathbf{X}$. Each pair of singular vectors is unique with respect to each other only up to a scaling factor $e^{j\theta}$ of unit modulus. For example, the pair of singular vectors $[\mathbf{w}_i, \mathbf{v}_i]$ is completely equivalent to $[-\mathbf{w}_i, -\mathbf{v}_i]$. In principle, any number of equivalent pairs can be constructed by varying θ. Also when dealing with real spaces, $\mathbf{X}^*$ is simply the transpose, i.e., $\mathbf{X}^{\mathbf{T}}$.

The DSVDC routine in LINPACK [55] was extensively used for computations of the singular value decomposition. The data $\mathbf{X}(z_j, t_k)$ were obtained by integrating for 512 sec with samples being collected at regular 1 sec intervals. The sampling time was governed by the characteristic time scale of the system. For example, a sampling time of 10 sec caused aliasing.

[1] M. C. Cross and P. C. Hohenberg, Rev. Mod. Phys. **65**, 851 (1993).

[2] T. Hogg and B. A. Huberman, IEEE Trans. Syst. Man Cybern. **21**, 1325 (1991).

[3] D. Auerbach, C. Grebogi, E. Ott, and J. A. Yorke, Phys. Rev. Lett. **69**, 3479 (1992).

[4] H. Gang and H. Kaifen, Phys. Rev. Lett. **71**, 3794 (1993).

[5] F. Qin, E. E. Wolf, and H. C. Chang, Phys. Rev. Lett. **72**, 1459 (1994).

[6] M. Holodniok, M. Kubíček, and M. Marek (unpublished).

[7] G. Chen, bibliography available from ftp: "uhoop.egr.uh.edu/pub/TeX/chaos.tex" (login name and password: both "anonymous").

[8] E. Ott, C. Grebogi, and J. A. Yorke, Phys. Rev. Lett. **64**, 1196 (1990).

[9] W. L. Ditto, S. N. Rauseo, and M. L. Spano, Phys. Rev. Lett. **65**, 3211 (1990).

[10] A. Azevedo and S. M. Rezende, Phys. Rev. Lett. **66**, 1342 (1991).

[11] T. Shinbrot, C. Grebogi, E. Ott, and J. A. Yorke, Phys. Rev. Lett. **65**, 3215 (1990).

[12] T. Shinbrot, W. Ditto, C. Grebogi, E. Ott, M. Spano, and J. A. Yorke, Phys. Rev. Lett. **68**, 2863 (1992).

[13] T. Shinbrot, C. Grebogi, E. Ott, and J. A. Yorke, Phys. Rev. A **45**, 4165 (1992).

[14] T. Shinbrot, C. Grebogi, E. Ott, and J. A. Yorke, Phys.

Lett. A **169**, 349 (1992).
[15] T. Shinbrot, C. Grebogi, E. Ott, and J. A. Yorke, Nature (London) **363**, 411 (1993).
[16] T. Shinbrot, Nonlinear Sci. Today **3**, 2 (1993).
[17] E. J. Kostelich, C. Grebogi, E. Ott, and J. A. Yorke, Phys. Rev. E **47**, 305 (1993).
[18] J. K. Bandyopadhyay, V. R. Kumar, and B. D. Kulkarni, AIChE J. **39**, 908 (1993).
[19] N. J. Mehta and R. M. Henderson, Phys. Rev. A **44**, 4861 (1991).
[20] K. Pyragas, Phys. Lett. A **170**, 421 (1992).
[21] S. Bielawski, D. Derozier, and P. Glorieux, Phys. Rev. E **49**, 971 (1994).
[22] R. Lima and M. Pettini, Phys. Rev. A **41**, 726 (1990).
[23] M. Pettini, in *Dynamics and Stochastic Processes*, edited by R. Lima, L. Streit, and R. V. Mendes (Springer-Verlag, New York, 1990), pp. 242–250.
[24] Y. Braiman and I. Goldhirsch, Phys. Rev. Lett. **66**, 2545 (1991).
[25] Y. S. Kivshar, F. Rödelsperger, and H. Benner, Phys. Rev. E **49**, 319 (1994).
[26] H. Herzel, Z. Angew. Math. Mech. **68**, 582 (1988).
[27] L. M. Pecora and T. L. Carroll, Phys. Rev. Lett. **64**, 821 (1990).
[28] L. M. Pecora and T. L. Carroll, Phys. Rev. A **44**, 2374 (1991).
[29] K. Pyragas, Phys. Lett. A **181**, 203 (1993).
[30] A. Kittel, K. Pyragas, and R. Richter, Phys. Rev. E **50**, 262 (1994).
[31] L. M. Hively, Fusion Technol. **24**, 127 (1993).
[32] D. H. Gay and W. H. Ray, Chem. Eng. Sci. **50**, No. 10, 1519 (1995).
[33] D. H. Gay and W. H. Ray, in *Proc. IFAC Workshop on Model-Based Process Control, Atlanta, GA*, edited by J. T. McAvoy, Y. Arkun, and E. Zafiriou (Pergamon, Oxford, 1988), pp. 95–102.
[34] C. Chen and H. Chang, AIChE J. **38**, 1461 (1992).
[35] L. Sirovich, Q. Appl. Math. **XLV**, 561 (1987).
[36] E. N. Lorenz, MIT Department of Meteorology Statistical Forecasting Project Technical Report No. 1, 1956 (unpublished).
[37] D. S. Broomhead and G. P. King, Physica D **20**, 217 (1986).
[38] M. Marek and I. Schreiber, *Chaotic Behaviour of Deterministic Dissipative Systems* (Cambridge University Press, Cambridge, England, 1991).
[39] M. Henon, Physica **5D**, 412 (1982).
[40] R. Brankin, I. Gladwell, and L. Shampine, Department of Mathematics, Southern Methodist University Report No. 92-S1, 19xx (unpublished).
[41] M. Caracotsios and W. E. Stewart, Comput. Chem. Eng. **9**, 359 (1985).
[42] L. R. Petzold, DDASSL Documentation, Sandia National Laboratories, Livermore, CA, 1983.
[43] G. W. Stewart, SIAM Rev. **35**, 551 (1993).
[44] K. Fukunaga, *Introduction to Statistical Pattern Recognition* (Academic Press, Inc., Boston, 1990).
[45] M. Kirby and D. Armbruster, Z. Angew. Math. Phys. **43**, 999 (1992).
[46] J. L. Lumley, *Stochastic Tools in Turbulence* (Academic Press, New York, 1970).
[47] G. Berkooz, P. Holmes, and J. L. Lumley, Annu. Rev. Fluid Mech. **25**, 539 (1993).
[48] M. D. Graham, S. L. Lane, and D. Luss, J. Phys. Chem. **97**, 889 (1993).
[49] N. Aubry, R. Guyonnet, and R. Lima, J. Stat. Phys. **64**, 683 (1991).
[50] H. Herzel, K. Krischer, D. Berry, and I. Titze (unpublished).
[51] M. Field and M. Golubitsky, *Symmetry in Chaos* (Oxford University Press, Oxford, 1992).
[52] W. H. Ray, *Advanced Process Control* (McGraw-Hill, New York, 1981).
[53] B. A. Ogunnaike and W. H. Ray, *Process Dynamics, Modelling and Control* (Oxford University Press, Oxford, 1994).
[54] M. D. Graham and I. G. Kevrekidis, Comput. Chem. Eng. (to be published).
[55] J. Dongarra, C. Moler, J. Bunch, and G. Stewart, *LINPACK Users' Guide* (SIAM, Philadelphia, 1979).